

Article

Preparation of High-Efficiency Fe/N-Doped Carbon Catalysts Derived from Graphite Phase Carbon Nitride for Reduction of Oxygen

Yan Wang^{1,2,3}, Wuxin Liu^{1,2,3}, Rongzhe Wang^{1,2,3}, Qing Wang^{1,2,3,4,*}, Shaohua Luo^{1,2,3,4,*}, Pengqing Hou^{3,4,5}, Yahui Zhang^{1,2,3,4}, Shengxue Yan^{1,2,3,4}, Xin Liu^{1,2,3,4} and Jing Guo^{1,2,3,4}

¹ School of Materials Science and Engineering, Northeastern University, Shenyang 110819, China; w15827311221@163.com (Y.W.); wxone0817@163.com (W.L.); m13131731112@163.com (R.W.); zh_yahui@neuq.edu.cn (Y.Z.); yanshengxueneu@163.com (S.Y.); liuxinnumber1@foxmail.com (X.L.); guojing@neuq.edu.cn (J.G.)

² State Key Laboratory of Rolling and Automation, Northeastern University, Shenyang 110819, China

³ Hebei Key Laboratory of Dielectric and Electrolyte Functional Material, Qinhuangdao 066004, China; 2008hpq@163.com

⁴ School of Resources and Materials, Northeastern University at Qinhuangdao, Qinhuangdao 066004, China

⁵ School of Materials Science and Engineering, Shenyang University of Technology, Shenyang 110870, China

* Correspondence: wangqing@neuq.edu.cn (Q.W.); luoshaohua@neuq.edu.cn (S.L.);

Tel.: +86-15032322691 (Q.W.); +86-13613349334 (S.L.)

Abstract: Fe/N-doped carbon (Fe-NC) is an excellent base-metal catalyst for use in an electrocatalytic oxygen reduction reaction (ORR) with high activity. In this paper, graphite phase carbon nitride (g-C₃N₄) was first obtained from the pyrolyzing of melamine, and then different proportions of FeCl₃ were separately doped into g-C₃N₄ to further prepare the Fe-NC catalyst. The Fe-NC catalyst was applied in an ORR reaction, and the results show that the Fe-NC catalyst doped with 0.5 mmol FeCl₃ possesses exceptional electrocatalytic performance, with an onset potential of 0.96 V and a half-wave potential of 0.81 V, which approaches that of a Pt/C catalyst. Meanwhile, the Fe-NC catalyst displays high stability and methanol resistance. The results supply a new way to prepare efficient ORR electrocatalysts.

Keywords: Fe-N-C; g-C₃N₄; doping; ORR



Citation: Wang, Y.; Liu, W.; Wang, R.; Wang, Q.; Luo, S.; Hou, P.; Zhang, Y.; Yan, S.; Liu, X.; Guo, J. Preparation of High-Efficiency Fe/N-Doped Carbon Catalysts Derived from Graphite Phase Carbon Nitride for Reduction of Oxygen. *Catalysts* **2024**, *14*, 279. <https://doi.org/10.3390/catal14040279>

Academic Editor: Ermete Antolini

Received: 26 March 2024

Revised: 13 April 2024

Accepted: 17 April 2024

Published: 19 April 2024



Copyright: © 2024 by the authors. Licensee MDPI, Basel, Switzerland. This article is an open access article distributed under the terms and conditions of the Creative Commons Attribution (CC BY) license (<https://creativecommons.org/licenses/by/4.0/>).

1. Introduction

With the increasingly prominent fossil resource crisis and global environmental issues, the development of new renewable green alternative energy has become an important measure for coping with global energy shortages and climate change [1–3]. In recent years, metal-air batteries have attracted a lot of attention in the field of electrochemistry because of the simplicity of operation, sustainability, environmental friendliness, and high efficiency. Among the existing metal-air batteries, the rechargeable zinc-air battery (ZABs) is widely regarded as one of the energy storage and conversion systems with the most potential, owing to its high energy density, reliability, environmental friendliness, and superior safety [4]. Oxygen reduction reaction (ORR) and oxygen extraction reaction (OER) are the two basic electrode reactions involved in ZABs [5]. However, the sluggish kinetics of ORRs on air cathodes leads to the low energy conversion efficiency output performance and long-cycle stability of zinc-air batteries; therefore, it is imperative to rationally design OER and ORR electrocatalysts with high activity [6,7]. Currently, the commonly used Pt/C electrocatalyst exhibits advantages in electrochemical performance, but poor OER activity due to the oxidation of Pt at high overpotentials, the shortage of precious metal resources, and the increase in cost still cannot completely solve the problem of cathodes for zinc-air batteries [2,8–10]. For these reasons, the large-scale commercial construction

and application of zinc-air batteries have always been seriously hindered. Therefore, developing efficient and stable base-metal catalysts is of great significance for improving the performance of zinc-air batteries [11].

A M-N-C catalyst formed by nitrogen-doped carbon-supported transition metal atoms (Fe, Co, etc.) is a class of highly efficient oxygen electrocatalysts [2,12–15]. Among them, the Fe-NC catalyst has attracted huge attention because of the activity of ORRs, such as a Pt-based catalyst [16–19]. Due to the uniform distribution of electron cloud density between C-C bonds, the ORR electrocatalytic activity and stability of the carbon materials are weakened. The N and Fe co-doping of carbon-based materials is beneficial as it can change the electron cloud density around C atoms, polarize the C atoms near the heteroatoms, and improve the electrocatalytic activity of ORR catalysts [20]. Meanwhile, N atoms have a higher electronegativity than C atoms, resulting in easier coordination between Fe and N when forming the catalytic active center FeN_x [21].

The high-temperature cracking of precursors containing metal Fe, N, and C is a traditional method for preparing Fe-NC [22–25]. In general, a high nitrogen content in the precursor is required in order to retain more nitrogen during the pyrolysis process and form highly nitrogen-doped carbon. Graphite phase carbon nitride ($\text{g-C}_3\text{N}_4$) is a typical carbon–nitrogen compound with a graphene-like lamellar structure. The poor electrical conductivity of $\text{g-C}_3\text{N}_4$ limits its direct application in the field of electrocatalysis. However, owing to its extremely high nitrogen content of up to 57.1 at%, $\text{g-C}_3\text{N}_4$ is an excellent precursor for synthesizing nitrogen-doped carbon materials. By doping iron salts, $\text{g-C}_3\text{N}_4$ can be converted into Fe and N co-doped electrocatalytic carbon-based materials.

In this paper, low-cost melamine is used to produce $\text{g-C}_3\text{N}_4$, followed by the addition of iron salts. The mixture is pyrolyzed at a high temperature in order to produce Fe-NC materials. Finally, Fe-NC is used as an electrocatalyst in the ORR reaction. The results show that Fe-NC exhibits outstanding electrocatalytic performance, approaching that of the commercial Pt/C catalyst. Meanwhile, Fe-NC also possesses an exceptional methanol resistance and long-term stability.

2. Results and Discussion

Figure 1 shows the preparation diagram of the Fe-NC catalyst. Melamine was first heated at $550\text{ }^\circ\text{C}$ and converted into $\text{g-C}_3\text{N}_4$. Subsequently, the as-obtained $\text{g-C}_3\text{N}_4$ was mixed with different proportions of $\text{FeCl}_3 \cdot 6\text{H}_2\text{O}$. Finally, the mixture was heated at $800\text{ }^\circ\text{C}$ to obtain the Fe-NC catalyst. The Fe-NC catalysts prepared by adding different amounts of iron salts were marked as Fe-NC-x (x indicates the amount of iron salt added; for example, Fe-NC-0.1 indicates the addition of 0.1 mmol $\text{FeCl}_3 \cdot 6\text{H}_2\text{O}$).



Figure 1. The preparation diagram of the Fe-NC catalyst.

The SEM and TEM of $g\text{-C}_3\text{N}_4$ are analyzed and shown in Figure 2a,b, from which it can be observed that the $g\text{-C}_3\text{N}_4$ formed via the heat treatment of melamine exhibits a blocky structure, which consists of irregular two-dimensional lamellae stacked on top of each other. The elemental composition and content of $g\text{-C}_3\text{N}_4$ were investigated using XPS and the results are shown in Figure 2c. From the figure, it can be discovered that $g\text{-C}_3\text{N}_4$ has a N content of up to 44%, close to the content of C. The rich nitrogen content of the precursor provides benefits when forming active centers. To better observe the morphology of nitrogen-doped carbon matrix-loaded Fe atoms, the SEM characterization of Fe-NC-0.1, Fe-NC-0.5, and Fe-NC-1.5 was performed, as shown in Figure 2d–f. From the figures, it can be seen that the lamellar $g\text{-C}_3\text{N}_4$ was transformed into elongated nanotubes carbon under the catalytic effect of Fe atoms [26], which is favorable for the improvement of the active site and mass transfer kinetics [27]. With the increase in the Fe content, the tubes gradually become clear and elongated. However, when the Fe doping amount reaches 1.5 mmol, the tubes gradually become blurred and decrease in number, which might be ascribed to the agglomeration triggered by the excessive Fe atoms, making the density of Fe single atoms decrease, and the catalytic performance weaken.

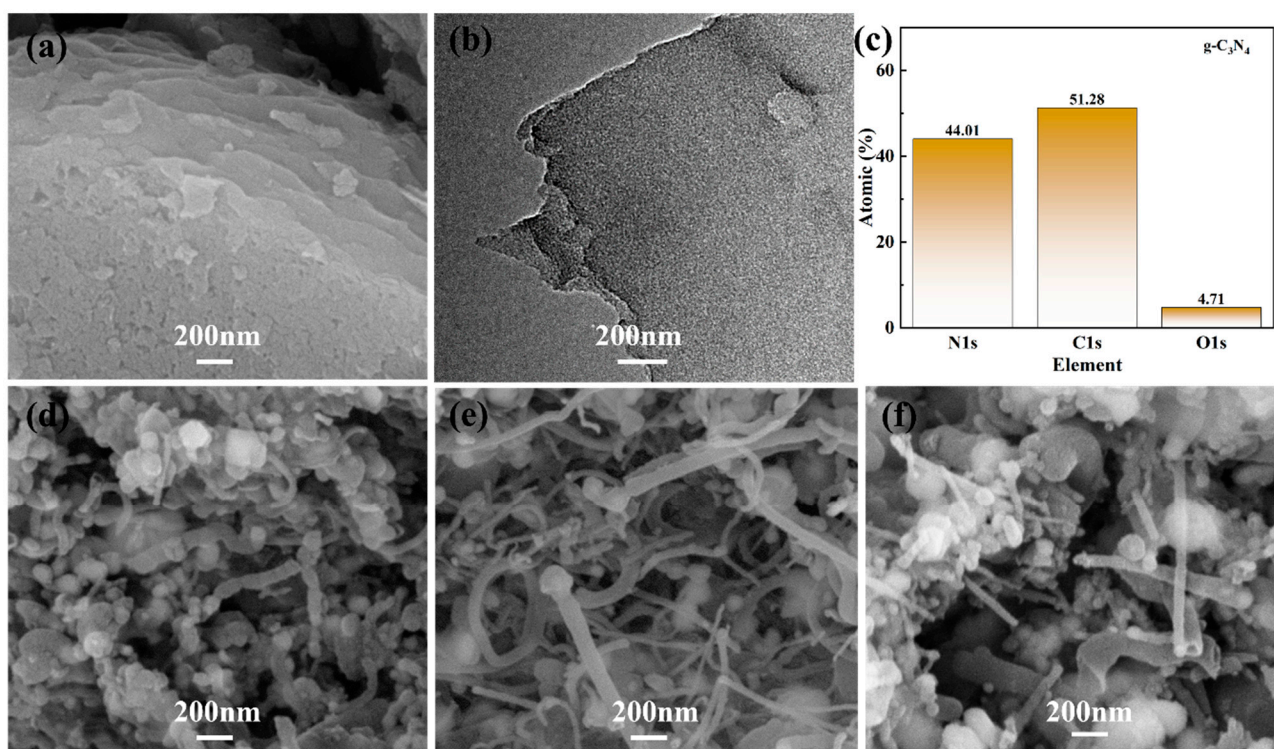


Figure 2. (a) SEM and (b) TEM image of $g\text{-C}_3\text{N}_4$. (c) XPS elemental content diagram of $g\text{-C}_3\text{N}_4$. (d–f) SEM image of Fe-NC.

Figure 3a–c show the TEM characterization of Fe-NC-0.1, Fe-NC-0.5, and Fe-NC-1.5, respectively. From the images, it can be seen that the different doping ratios all form a folded tubular morphology. The Fe-NC-0.1 and Fe-NC-0.5 samples have a clear tubular morphology with clear walls, but the walls of the Fe-NC-1.5 sample become blurred and lack a clear boundary. In addition, black Fe nanoparticles are observed in all Fe-NC samples, some of which are encapsulated in intertwined tubes, and some are located in the outer tube walls. The size of the nanoparticles becomes progressively larger as the amount of iron doping increases, indicating increasingly severe Fe agglomeration. In addition, the holes in the tube are irregular and almost invisible. To determine the material structure and composition of the Fe-NC catalyst, the Fe-NC-0.5 sample was characterized using HRTEM and fast Fourier inverse transform (FFT). As can be seen in Figure 3d,e, the largest layer spacing of 0.346 nm should correspond to the (002) facets of graphite, the layer spacing

of 0.201 nm is attached to the Fe_3C substance, and the smallest layer spacing of 0.193 nm reflects the (110) facets of the $\alpha\text{-Fe}$.

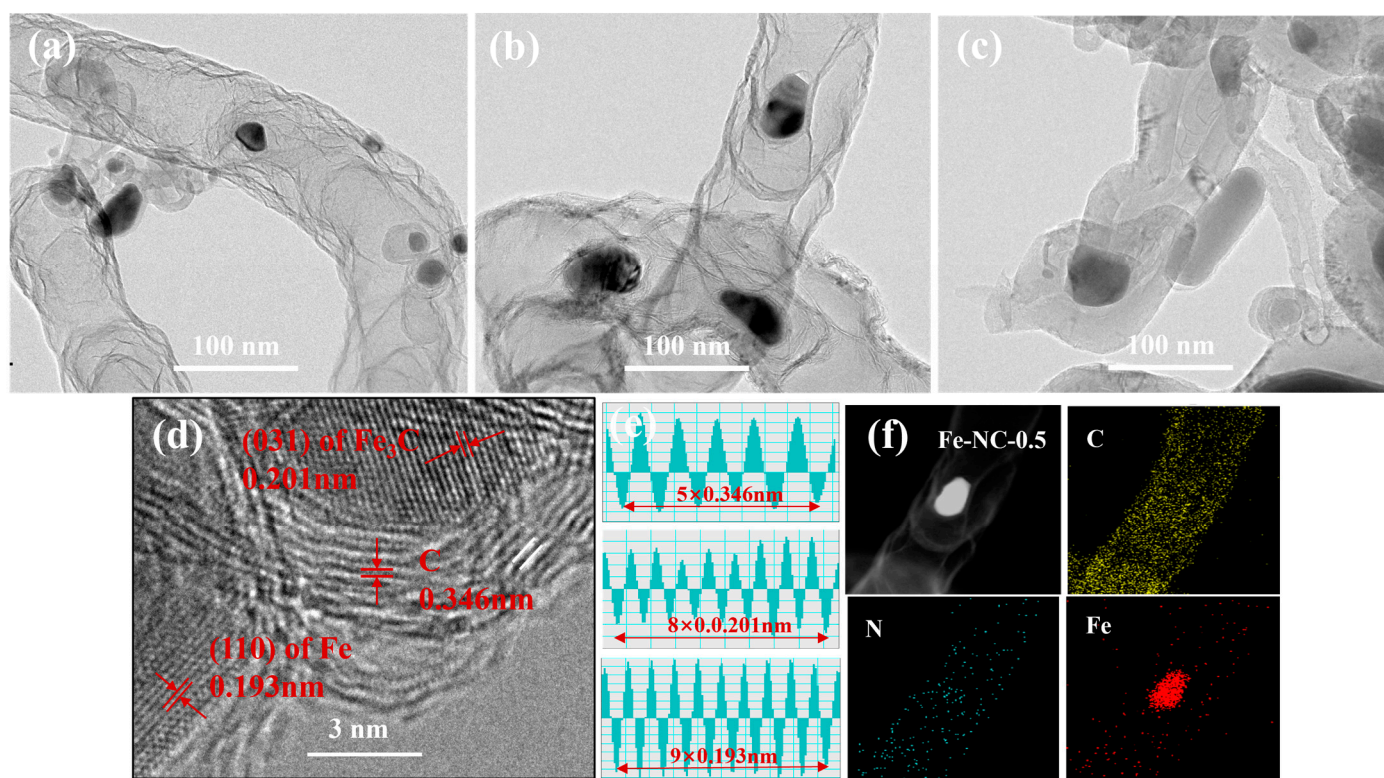


Figure 3. (a–c) TEM image of the Fe-NC-0.1, Fe-NC-0.5, and Fe-NC-1.5, respectively. (d) HRTEM of the Fe-NC-0.5. (e) Line scan of the FFT. (f) TEM image of the Fe-NC-0.5 and homologous elemental maps of C, N, and Fe, respectively.

The elemental distribution scanning mapping of Fe-NC-0.5 (Figure 3f) reveals that both C and N are uniformly distributed throughout the sample, indicating the generation of N-doped carbon. Iron atoms are distributed inside nitrogen-doped carbon nanotubes, suggesting that the iron is doped in the carbon.

The XRD patterns of all the samples are shown in Figure 4a. From the XRD pattern of $g\text{-C}_3\text{N}_4$, it can be seen that there are two diffraction peaks at 13.2° and 27.4° , which belong to the (100) and (002) facets of the $g\text{-C}_3\text{N}_4$, respectively. After the addition of $\text{FeCl}_3 \cdot 6\text{H}_2\text{O}$ and the second calcination at 800°C , a series of diffraction peaks at 44.7° , 43.8° , 45.8° , and 26.2° appeared in the XRD spectrum. The strong peak at 44.7° represents diffraction from the Fe_3C substance. The peak at 43.8° is generated by the diffraction of the (111) facet of hexagonal $\epsilon\text{-Fe}_3\text{N}$. The weak and broad peak at 26.2° might be the (002) crystal facet of carbon, and the peak at 45.8° should be the (110) crystal facet of Fe. In addition, some small weak peaks might be attributed to Fe_3C , but it is debatable whether they are catalytically active or not [28]. According to the literature [21,29], through high-temperature treatment, FeC_xN_y or FeN_x might also be formed due to the interactions between Fe, N, and C. In ORRs, FeC_xN_y or FeN_x molecules with $\alpha\text{-Fe}$ and $\epsilon\text{-Fe}_3\text{N}$ constitute the electrocatalytic active center [30,31].

The Raman spectra of pure $g\text{-C}_3\text{N}_4$ and Fe-NC catalysts are displayed in Figure 4b. From the figure, it can be seen that $g\text{-C}_3\text{N}_4$ shows only a high intensity noise line. All Fe-NC materials exhibit two strong characteristic peaks near 1350 cm^{-1} and 1580 cm^{-1} , belonging to the disordered carbon bands (D-band) and graphitic carbon bands (G-band), respectively [22]. This indicates that $g\text{-C}_3\text{N}_4$ is converted to carbon under pyrolysis at 800°C . The intensity area ratio (I_D/I_G) of the two bands reflects the disorder degree in the carbon structure [32]. The high I_D/I_G ratio implies a high degree of disorder in carbon. As

the amount of Fe added increases, the I_D/I_G value of the Fe-NC material decreases from 1.06 to 0.92, indicating an increase in the graphitization degree of carbon. The reason for this is that the heterogeneous catalytic effect of Fe reduces the activation energy for the transition from the amorphous to the graphite phase, thus promoting an increase in the graphitization. In addition, higher I_D/I_G values indicate the presence of a large amount of defects in the samples caused by N doping, and the defects can then become the catalytic active center [33,34].

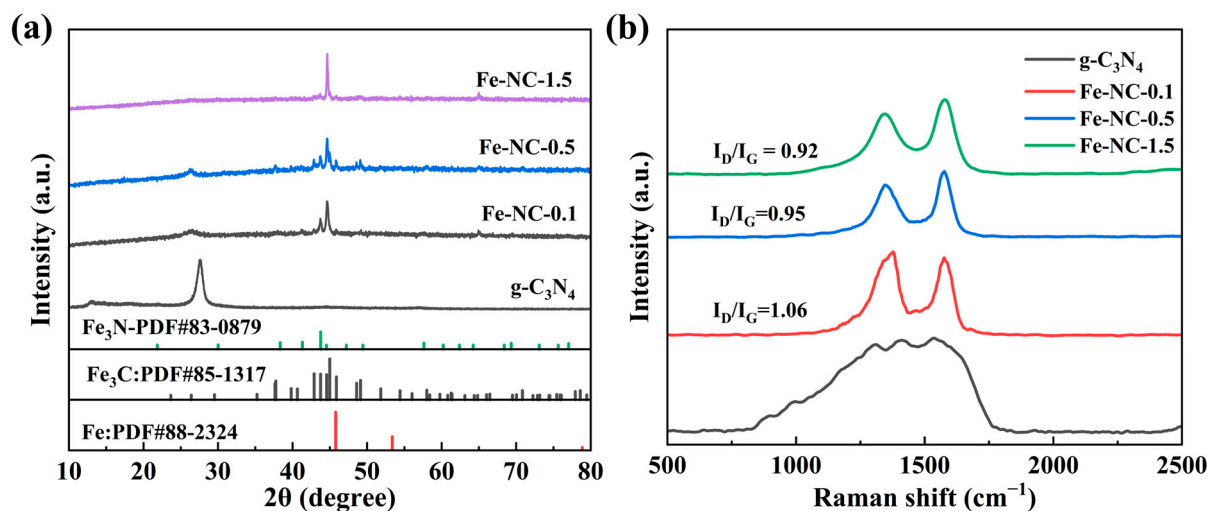


Figure 4. (a) XRD patterns, (b) Raman spectra of the samples.

The specific surface area and pore structures of the three samples were detected utilizing a nitrogen adsorption/desorption technique. Figure 5 reveals the nitrogen adsorption and desorption curves of the three samples and the corresponding pore diameter distribution. It can be seen from the figures that the specific surface areas of Fe-NC-0.1, Fe-NC-0.5, and Fe-NC-1.5 are 52.9, 89.2, and 41.6 $\text{m}^2 \text{g}^{-1}$, respectively. The high surface area can supply more active sites. In addition, the figure shows that the three samples make up the hierarchical distribution of micropores and mesopores, providing a favorable material transport channel for ORR reactions.

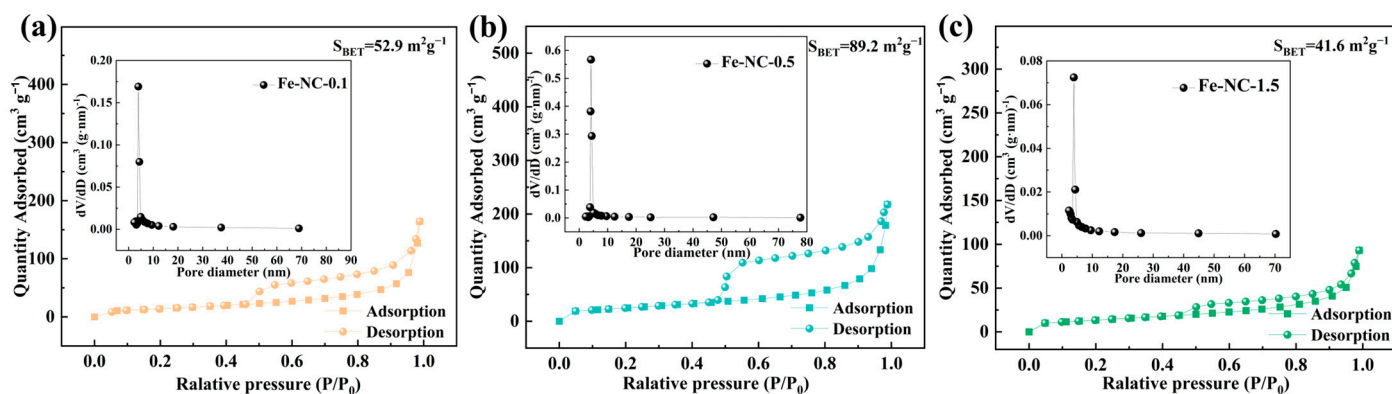


Figure 5. (a–c) BET images of the Fe-NC-0.1, Fe-NC-0.5, and Fe-NC-1.5, respectively.

XPS was used to analyze the surface chemical elements and binding states of all samples (Figure 6). As displayed in Figure 6a, the total XPS spectra reveal the existence of C, N, Fe, and O elements in all of the samples, where the presence of O could be attributed to the exogenous oxygenated compounds adsorbed on the surface. As can be seen in Figure 6b, the Fe-NC-0.5 sample has the highest N and O content among all the samples. The C1s spectra of

the Fe-NC samples in Figure 6c,f,i can be divided into four peaks, representing the telescopic vibrations of C=C/C-C (284.5 eV), C=N (285.3 eV), C-O (286.5 eV), and C=O (289.0 eV), respectively [22,31]. The relatively strong peak intensity corresponding to C=N suggests more N doping in the carbon. From Figure 6d,g,j, the N1s spectra can be divided into four peaks located at 398.2, 400.3, 401.3, and 404.0 eV. Among them, the peaks at 400.3, 401.3, and 404.0 eV represent pyrrole N, graphitized N, and quaternary N, respectively, whereas the peak situated at 398.2 eV represents the pyridine N and Fe-N [35–37]. According to the literature [38], the N group-modified conductive surfaces are able to provide binding sites because the active sites are generated on the surfaces via metal–nitrogen coordination. In addition, the ORR activity of N-doped catalysts is also affected by the content of pyridine and graphitized N. It is generally considered that pyridine N and graphitized N might promote oxygen-selective reduction through a four-electron mechanism [37,39,40]. Table 1 displays the nitrogen contents of all three catalysts. The contents of pyridine N and graphitized N in Fe-NC-0.5 accounted for 84.7% of the total peak content, slightly higher than those found in Fe-NC-0.1 and Fe-NC-1.5, which was conducive to the enhancement of active sites and electrical conductivity, thus promoting the ORR reaction. Figure 6e,h,k show the detailed valence states of Fe elements in Fe-NC compounds. The peaks situated at 706.8 eV and 707.3 eV belong to Fe₃N and metallic Fe, respectively [29]. The peaks at 720.3 eV and 710.1 eV belong to the Fe²⁺ states pertaining to Fe 2p_{1/2} and Fe 2p_{3/2} [23]. The peak situated at 723.4 eV represents the Fe³⁺2p_{1/2}, and another peak located at 712.3 eV indicates the Fe³⁺2p_{3/2} [41]. Since no iron oxides were discovered in XRD, the Fe²⁺ and Fe³⁺ should stem from the existence of FeC_xN_y and FeN_x [42].

Table 1. Different peak contents of C1s by XPS.

Samples	Quarternary-N (%)	Graphitic-N (%)	Pyrrolic-N (%)	Pyridinic-N (%)
0.1 Fe	7.97	22.59	13.69	55.74
0.5 Fe	8.42	28.27	6.88	56.43
1.5 Fe	6.71	27.37	11.72	54.21

To analyze the ORR performances of all catalysts, cyclic voltammetry (CV) curves were operated in a three-electrode system using the rotating electrode method in an oxygen-free/oxygen-saturated 0.1 M KOH alkaline electrolyte, as displayed in Figure 7. In the oxygen-saturated electrolyte, all the fabricated electrocatalysts except g-C₃N₄ show obvious ORR peaks. Among them, the oxygen reduction peak of Fe-NC-0.5 is the most obvious, and the oxidation peak appears in the oxygen-saturated CV curve at about 0.9 V, indicating that the redox reactions occurred between Fe(II) and Fe(III) in the existence of O₂. No ORR peaks were found in the oxygen-free saturated electrolyte, which also proved the catalyst's capability of oxygen reduction. In addition, both the Fe-NC-0.5 and Fe-NC-1.5 samples show reversible and featureless wide dual-layer charging current profile characteristics under an oxygen-free medium, thus implying good electronic conductivity and charge diffusion [43].

The ORR performance of Fe-NC catalysts with different Fe doping levels in the oxygen-saturated 0.1 M KOH solution was further investigated using linear scanning voltammetry (LSV) on an RDE at 1600 rpm, and the electrochemical parameters related to the ORR performance are shown in Figure 8 and Table 2. As can be observed from the data in Table 2, Fe-NC-0.5 has the best electrocatalytic property, with an onset potential (E_{onset}) of 0.96 V, a half-wave potential ($E_{1/2}$) of 0.81 V, and a limiting current density (J_d) of 5.97 mA cm⁻², which is close to that of Pt/C. In the same conditions, the catalytic activities of Fe-NC-0.1 (E_{onset} = 0.92 V, $E_{1/2}$ = 0.76 V, and J_d = 4.6 mA cm⁻²) and Fe-NC-1.5 (E_{onset} = 0.88 V, $E_{1/2}$ = 0.77 V, and J_d = 4.14 mA cm⁻²) are relatively low. The results might prove the key role of metal Fe in the catalyst. Among these catalysts, Fe-NC-0.5 has the lowest surface nitrogen content, but shows the best ORR performance, probably because Fe plays a more critical catalytic role. The doping of Fe provides single-atom active sites, but the excessive

doping of Fe might result in severe agglomeration, forming large-sized particles, which leads to a decrease in the density of Fe single atoms [44].

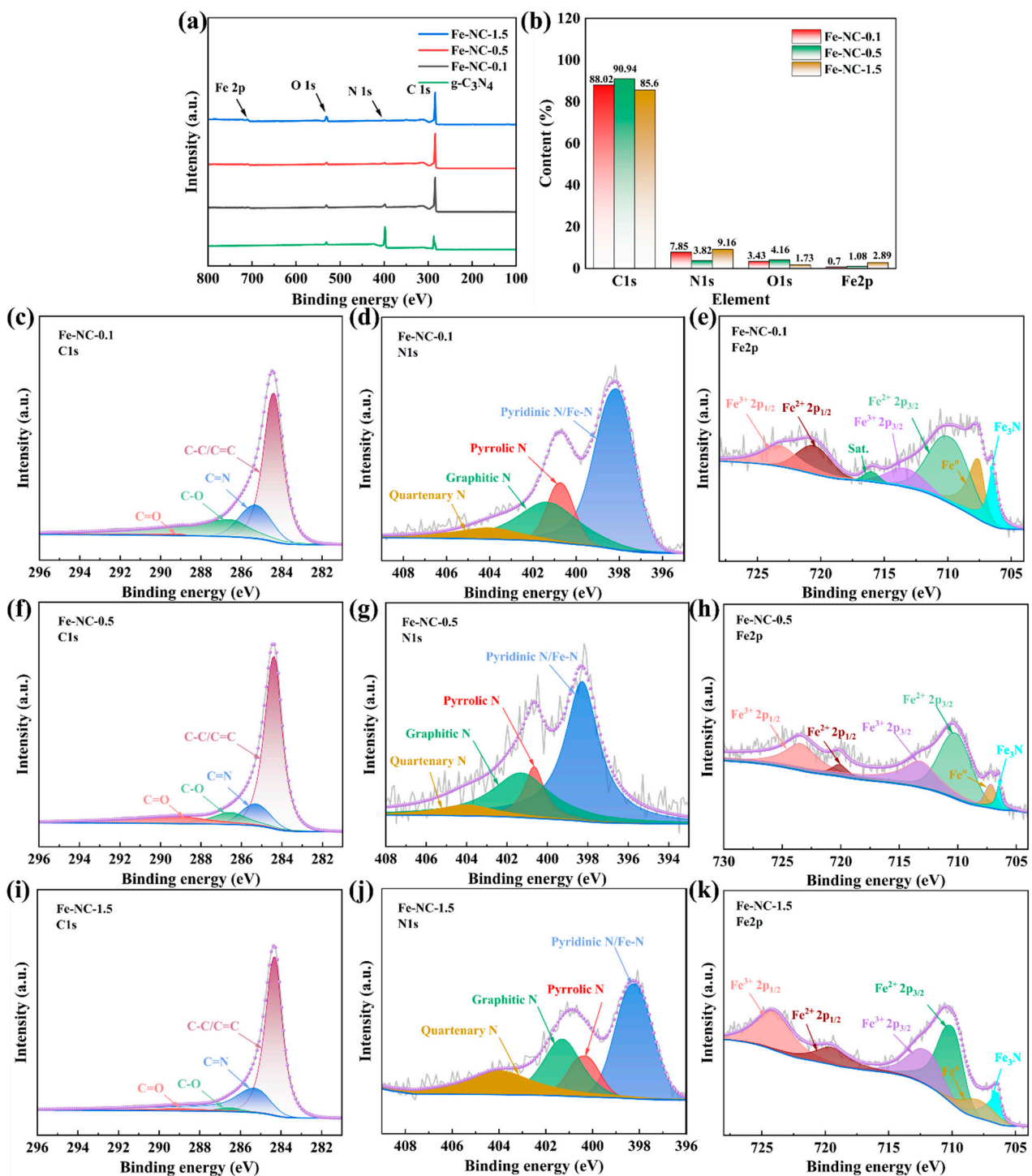


Figure 6. (a) Full XPS spectra of three catalysts and g-C₃N₄. (b) Elemental change diagrams of three catalysts. (c,f,i) C1s, (d,g,j) N1s, and (e,h,k) Fe 2p XPS spectra of three catalysts.

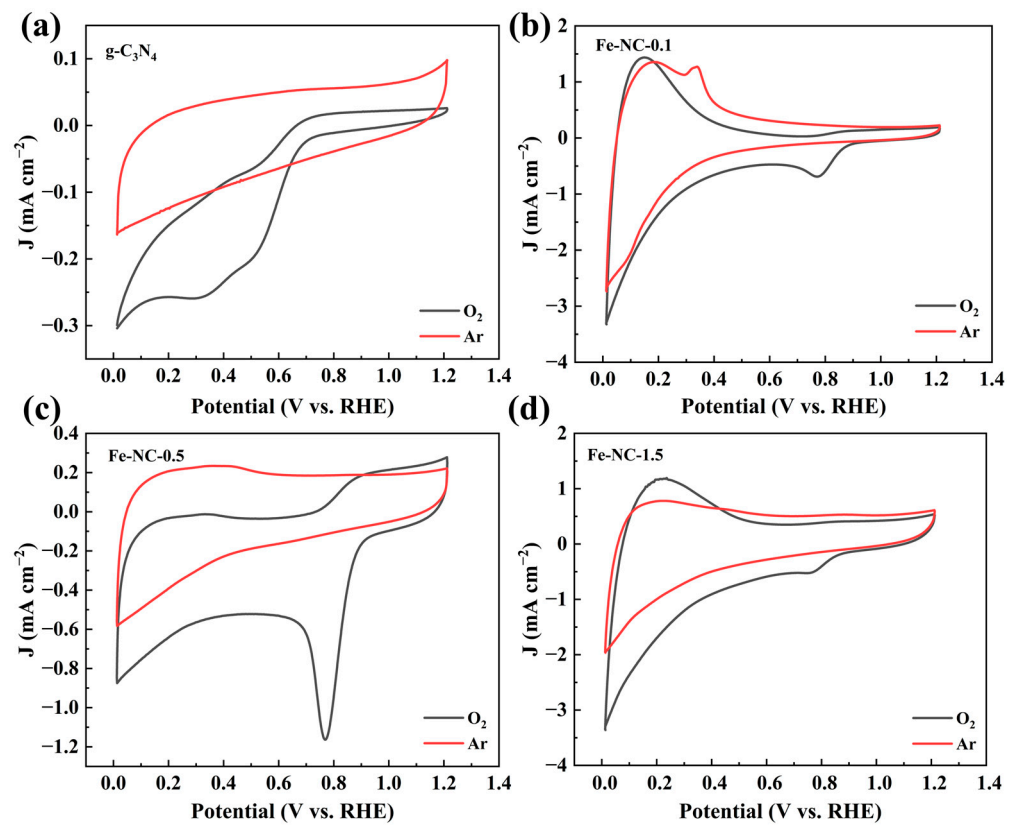


Figure 7. (a) CV curves of g-C₃N₄. (b–d) CV curves of Fe-NC-0.1, Fe-NC-0.5, Fe-NC-1.5, respectively.

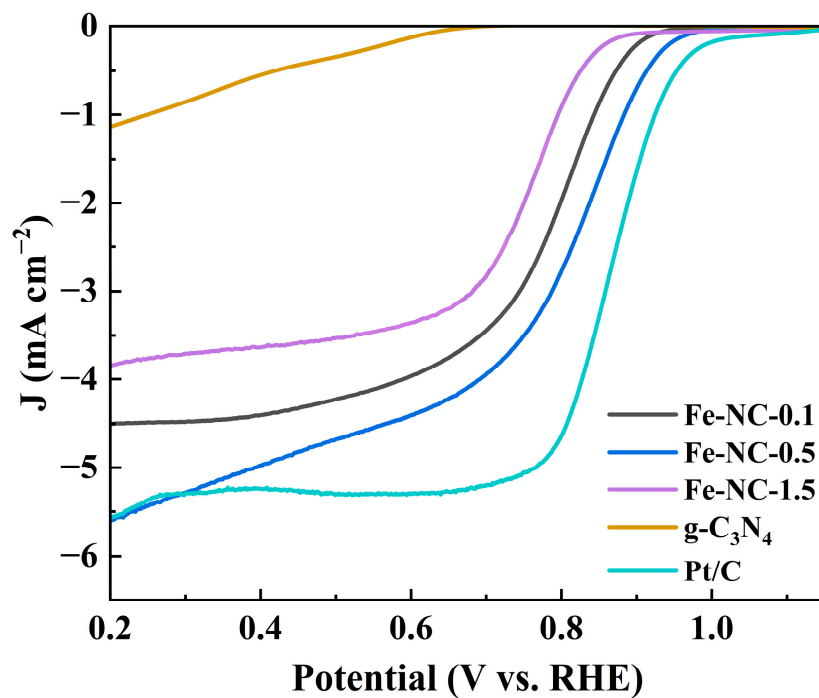


Figure 8. LSV curves of five catalysts.

Table 2. ORR properties of different catalysts.

Samples	Onset Potential (E_{onset} V)	Half-Wave Potential ($E_{1/2}$ V)	Limiting Current Density (mA cm^{-2})	Electron Transfer Number (n)
0.1 Fe	0.92	0.76	4.6	3.81
0.5 Fe	0.96	0.81	5.97	3.90
1.5 Fe	0.88	0.77	4.14	3.89
Pt/C	0.98	0.84	5.48	—
g-C ₃ N ₄	0.69	—	1.4	—

The LSV curves and K-L plots of the Fe-NC catalysts at different rotational speeds were conducted and displayed in Figure 9. From Figure 9a,c,e, it can be discovered that the current density enhances significantly when the rotational speed increases. The charge transfer numbers were calculated from the slope of the j^{-1} vs. ω^{-1} curves according to the Koutecky–Levich (K-L) equation. As revealed in Table 2, the charge transfer numbers of Fe-NC-0.1, Fe-NC-0.5, and Fe-NC-1.5 catalysts are 3.81, 3.90, and 3.89, respectively. The results indicate that these catalysts undergo four-electron reactions during oxygen reduction. Among them, Fe-NC-0.5 has the largest number of electrons transferred and the fastest four-electron reaction rate.

The reaction kinetics were further explored via the analysis of the polarization curves of all catalysts at 1600 rpm through the Tafel equation. As shown in Figure 10a,b, the Tafel slopes of Fe-NC-0.1, Fe-NC-0.5, and Fe-NC-1.5 are 93, 68, and 94 mV dec^{-1} , respectively. The smaller the Tafel slope, the faster the current density can increase as the change in overpotential decreases. The smallest slope for Fe-NC-0.5 indicates its outstanding electrocatalytic kinetics. The stability of the Fe-NC-0.5 catalyst was detected in an oxygen-saturated 0.1 M KOH electrolyte (0.4 V at 1600 rpm). From Figure 10c, it can be seen that there is no significant change in the polarization curve of Fe-NC-0.5 after 5000 cycles, which confirms the outstanding stability of the prepared Fe-NC-0.5. To test the methanol resistance of the catalyst, the LSV curves of Fe-NC-0.5 in the solution with or without methanol are compared and displayed in Figure 10d. It can be seen that no significant differences occurred between the two LSV curves, thus indicating the excellent methanol tolerance of the Fe-NC-0.5 catalyst.

The electrochemical dual layer capacitance (Cdl) can be used to calculate the effective surface area involved in an electrochemical reaction, called the electrochemical active area (ECSA). In electrochemical reactions, a larger active surface area indicates the higher utilization of active sites. The linear fitting of the electrochemical double-layer capacitance is conducted via measuring the non-Faraday interval double-layer capacitance currents at different scan rates. The central potential used for the study is 0.1 V, with a potential range of 50 mV and scanning rates of 10 mV s^{-1} , 20 mV s^{-1} , 30 mV s^{-1} , and 50 mV s^{-1} . By plotting the charging current density difference ($\Delta J = J_{\text{anode}} - J_{\text{cathode}}$) against the scan rate, the corresponding slope is twice that of Cdl, meaning the electrochemically active area can be represented by the corresponding slope. Figure 11a–d shows the CV curves of the four catalysts at different sweep speeds, which were linearly fitted to obtain Figure 11e. From Figure 11e, the slopes of Fe-NC-0.1, Fe-NC-0.5, and Fe-NC-1.5 are 1.35, 4.51, and 0.19 mF cm^{-2} , respectively. The largest slope for Fe-NC-0.5 indicate a larger electrochemically active area, improving its catalytic activity.

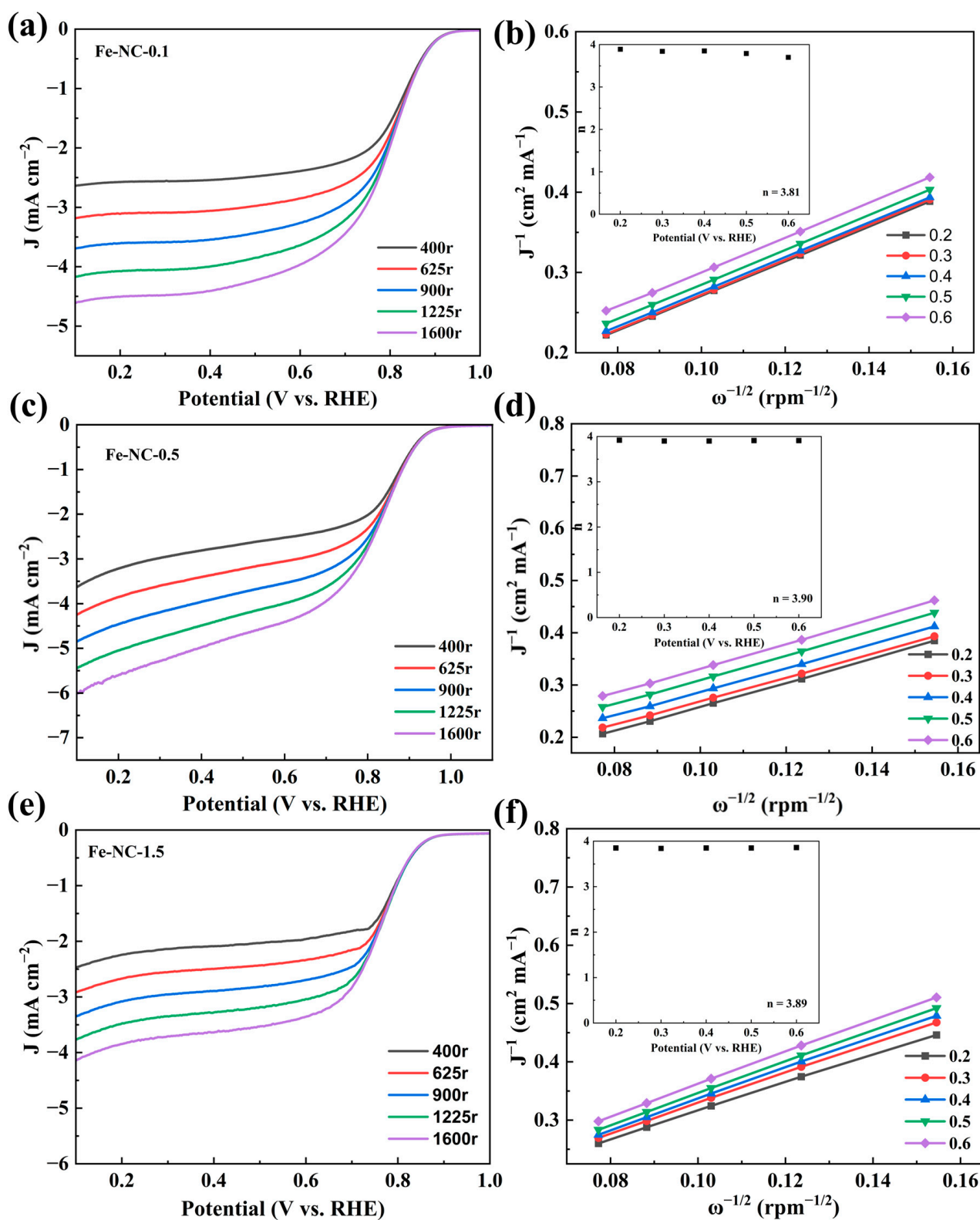


Figure 9. (a,c,e) LSV curves of three F-NC catalysts measured from 400–1600 rpm. (b,d,f) Charge transfer numbers and K-L plots.

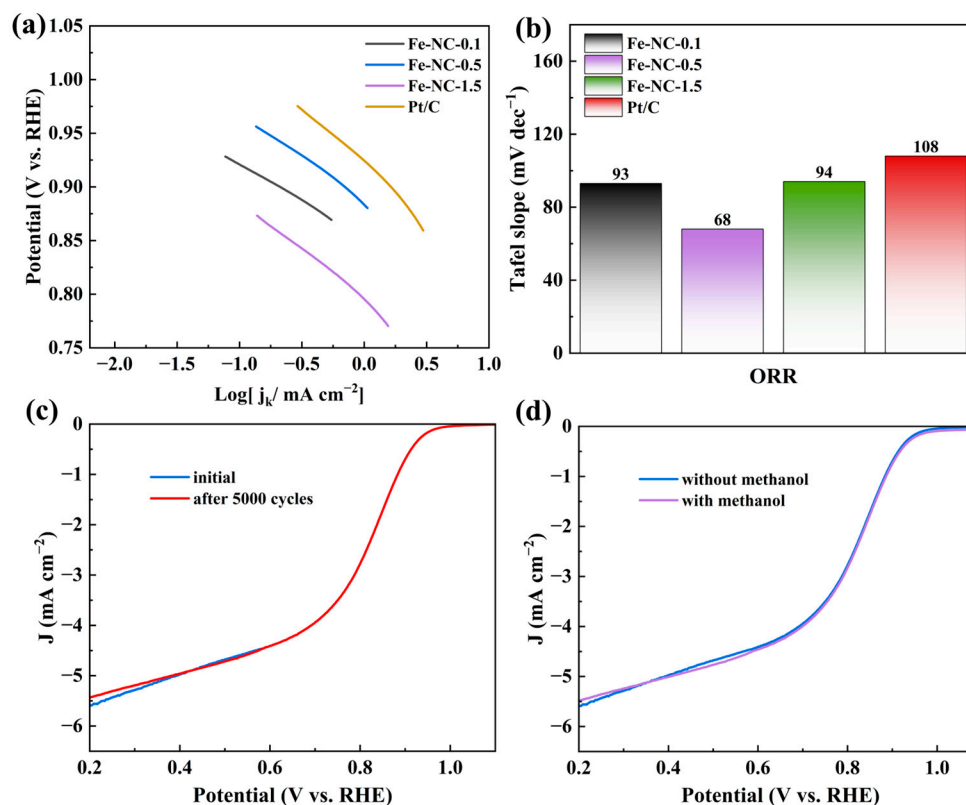


Figure 10. (a) Tafel plots of three F-NC catalysts and Pt/C obtained from the LSV at 1600 rpm. (b) Tafel slope histogram of three F-NC catalysts and Pt/C. (c) LSV curves of the first cycle and 5000 cycles later. (d) LSV curves of the F-NC-0.5 both with and without methanol.

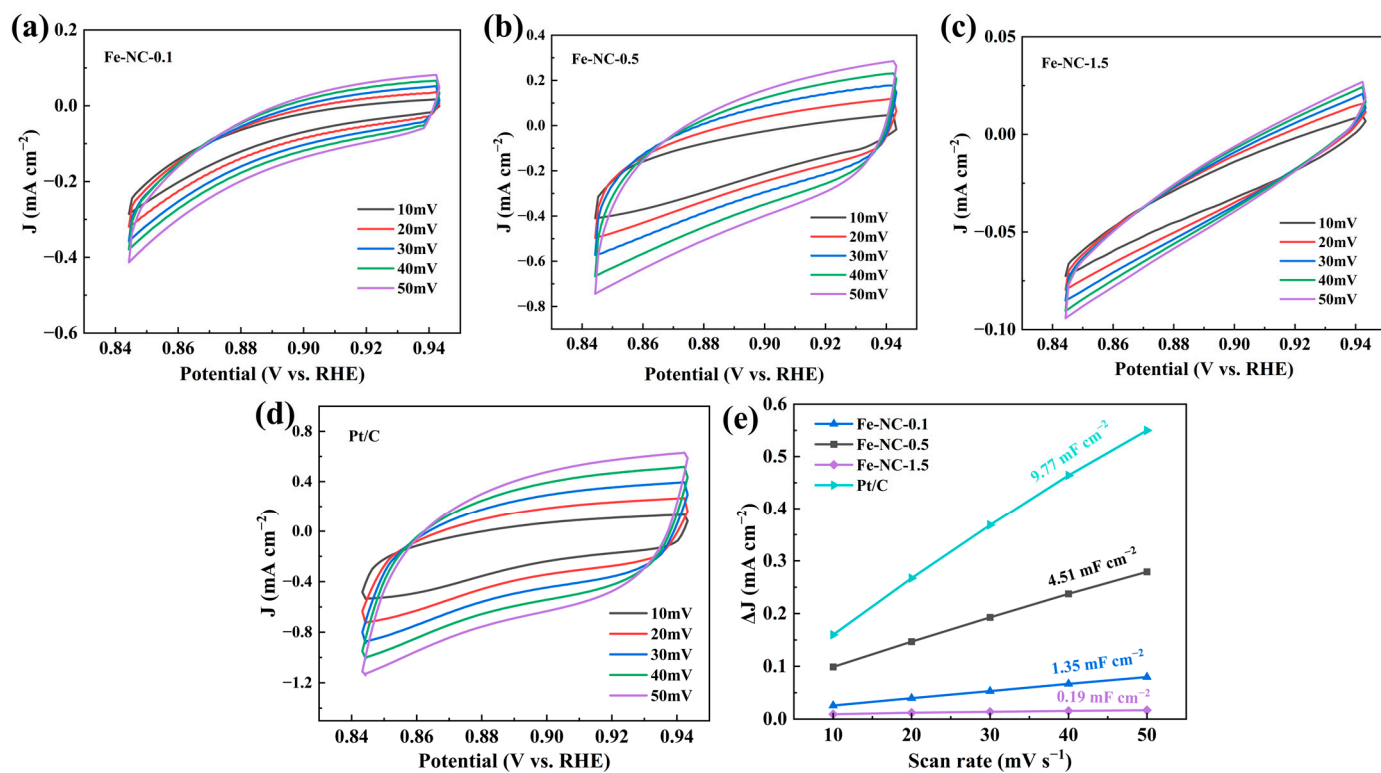


Figure 11. (a–d) ECSA curve comparisons of four catalysts. (e) The pattern is based on the difference in the charging current density and scanning rate.

The excellent ORR performance of the Fe-NC-0.5 catalyst could be ascribed to several reasons. Firstly, the N doping in the catalyst derived from g-C₃N₄ provides more surface defects and catalytically active sites, thus promoting the ORR reaction. In addition, by changing the electron cloud density, N activates the adjacent C atoms, increasing the electron transfer from metal atoms to carbon atoms and generating high catalytic activity. Secondly, the catalytic effect of Fe increases the graphitic degree of carbon materials, which is conducive to the improvement of electronic conductivity. Thirdly, the nanotube structures of carbon are beneficial for improving the mass transfer (such as O₂, H₂O, and intermediate products), which then enhances the reaction kinetics in the ORR reaction. Fourthly, the relatively high specific surface area also increases the exposure of the active site and thus enhances the catalytic activity. Finally, the formation of α-Fe, Fe₃N, FeC_xN_y, or FeN_x from the interactions between Fe, N, and C further enhances the active sites of the ORR reaction. In summary, the synergistic effect of multiple factors leads to excellent electrochemical performance of Fe-NC-0.5 catalysts.

3. Materials and Methods

3.1. Chemicals and Materials

Melamine (C₃H₆N₆) was obtained from Sinopharm Chemical Reagent Co., Ltd., Shanghai, China. Ferric chloride hexahydrate (FeCl₃·6H₂O) and potassium hydroxide (KOH) were gained from Aladdin Bio-technology Co., Ltd., Shanghai, China. The Nafion solution (C9HF17O5S.5%) was purchased from DuPont, Wilmington, DE, USA, and the platinum carbon (Pt/C, 20%) was purchased from Johnson Matthey Company (London, UK). All chemical reagents utilized in this experiment were of an analytical grade. The entire experiment was carried out using deionized water.

3.2. Preparation of Fe-NC Catalysts

Firstly, melamine was heated to 550 °C under an argon atmosphere at an elevated rate of 5 °C/min and kept for 4 h; in turn, a light-yellow g-C₃N₄ powder was gained. Furthermore, 2 g g-C₃N₄ was mixed with 0.1, 0.5, and 1.5 mmol of FeCl₃·6H₂O, respectively, and then immersed in a beaker containing 80 mL of deionized water and 20 mL of ethanol solution, followed by drying at 80 °C. The mixture was heated at 800 °C in a tube furnace (Henan Fryer Instrument Co., Luoyang, China), and then held for 2 h to obtain the Fe-NC catalyst. The Fe-NC catalysts with different Fe doping amounts were named Fe-NC-0.1, Fe-NC-0.5, and Fe-NC-1.5, respectively.

3.3. Characterization of Materials

The microstructure and morphology of the samples were studied using scanning electron microscopy (SEM, SUPRA-55, Carl Zeiss AG, Oberkochen, German) and transmission electron microscopy (TEM, FEI-Tecnaï G2 F20, Hillsboro, OR, USA). The phase structure was investigated via an X-ray powder diffraction (XRD, model: Smartlab X-ray diffractometer (Rigaku, Akishima, Japan) with Cu-Kα radiation, wavelength: λ = 0.15406 nm, scanning: angle 2θ ranging from 10 to 80°) technique. The phase structures of the samples were further detected via the use of Raman spectroscopy (HORIBA Scientific Lab RAM HR Evolution, Kyoto, Japan). X-ray photoelectron spectroscopy (XPS, ESCALAB 250Xi, ThermoFischer, Waltham, MA, USA) was utilized to investigate the elemental composition and valence states of the sample surfaces, and the measured data were analyzed using Thermo Avantage 5.9931.

3.4. Electrochemical Measurements

The electrochemical property of the catalyst in the ORR was tested on a CHI760E electrochemical workstation (CH Instruments, Bee Cave, TX, USA) with a three-electrode system. Graphite is a counter electrode, with reference electrodes of a modified glassy carbon disk electrode (RDE, 0.19625 cm^{−2}) and a saturated calomel electrode (SCE). The working electrode was in argon- and oxygen-saturated 0.1 M KOH electrolyte. The mixture

of the 2 mg Fe-NC catalyst, 100 μL deionized water, 95 μL anhydrous ethanol, and 5 μL of Nafion solution (5 wt%) was sonicated for 2 h. Subsequently, 10 μL of the mixture (at a concentration of about 0.5 mg cm^{-2}) was dropped onto the working electrode. The electrolyte was filled with oxygen or argon for 30 min before testing. Cyclic voltammetry (scanning speed of 50 mV s^{-1} , voltage range from -1.0 V to 0.2 V) and linear scanning voltammetry (scanning speed of 10 mV s^{-1} , rotational speed from 400 to 1600 rpm) were then tested on the RDE. The ORR performance of commercial 20% Pt/C electrodes was also tested in order to compare with the performance of the Fe-NC catalysts. The LSV curves were compared before and after 5000 cycles to assess the durability of the catalyst (voltage 0.4 V, speed 1600 rpm). LSV was performed in 0.1 M KOH + 3 M methanol solution to assess the tolerance of the catalyst to methanol. The charge transfer number of the Fe-NC catalyst can be calculated using the Koutecky–Levich equation [29,45]:

$$\frac{1}{J} = \frac{1}{J_L} + \frac{1}{J_K} = \frac{1}{B\omega^{1/2}} + \frac{1}{J_K}$$

$$B = 0.62nFC_0D_0^{2/3}\nu^{-1/6}$$

where J represents the current density, J_L denotes the diffusion current density, J_K stands for the kinetic current density, ω represents the rotation rate of the RDE, F is Faraday's constant (96,485 C mol^{-1}), C_0 is the volumetric concentration of O_2 in oxygen-saturated 0.1 M KOH, D_0 is the diffusion coefficient of O_2 , ν denotes the kinetic viscosity, and n is the number of charge transfers that can be calculated based on the slope of the K-L plot.

4. Conclusions

In this paper, g- C_3N_4 was first synthesized with pyrolyzing melamine and then converted to a series of Fe-NC catalysts through mixing with $\text{FeCl}_3 \cdot 6\text{H}_2\text{O}$ and a calcination process. Among them, the Fe-NC-0.5 catalyst exhibits outstanding performance with E_{onset} potential of 0.96 V and $E_{1/2}$ potential of 0.81 V, respectively, which are significantly higher than those of the Fe-NC-0.1 and Fe-NC-1.5 catalysts. In addition, Fe-NC-0.5 exhibits high catalytic stability and an excellent methanol tolerance. These results express that the Fe-NC-0.5 catalyst is a prospective candidate material for ORR electrocatalysis. The conspicuous ORR property of Fe-NC-0.5 is ascribed to its rich surface defects derived from N doping, nanotube structures, the increased degree of graphitization, and the formation of multiple active centers, such as $\alpha\text{-Fe}$, $\varepsilon\text{-Fe}_3\text{N}$, FeC_xNy , or FeN_x .

Author Contributions: Conceptualization, W.L., Q.W. and S.L.; Methodology, Y.Z.; Validation, R.W.; Formal analysis, P.H.; Investigation, S.Y.; Writing—original draft, Y.W. and W.L.; data curation, W.L.; Writing—review & editing, Q.W.; Resources, X.L. and J.G. All authors have read and agreed to the published version of the manuscript.

Funding: This work was financially supported by the National Natural Science Foundation of China (No. 52104291, 52274295 and 52304325), the Natural Science Foundation of Hebei Province (No. E2021501007, E2021501029, E2022501029, E2022501028, and E2023501016), the Natural Science Foundation-Steel, the Iron Foundation of Hebei Province (No. E2022501030), the Science and Technology Project of Hebei Education Department (No. ZD2022158 and QN2024238), the Central Guided Local Science and Technology Development Fund Project of Hebei Province (No. 226Z4401G), the Fundamental Research Funds for the Central Universities (N2223010, N2223009 and N2323013), Performance subsidy fund for Key Laboratory of Dielectric and Electrolyte Functional Material Hebei Province (No. 22567627H). Qinhuangdao Science and Technology Research and Development Plan Project (No. 202302B046 and 202302B006).

Data Availability Statement: Data available on request due to restrictions, e.g., privacy or ethical. The data presented in this study are available on request from the corresponding author.

Conflicts of Interest: The authors declare that they have no known competing financial interests or personal relationships that could have appeared to influence the work reported in this paper.

References

1. Yang, W.X.; Zhang, Y.Q.; Liu, C.Y.; Jia, J.B. Dual-doped carbon composite for efficient oxygen reduction via electrospinning and incipient impregnation. *J. Power Sources* **2015**, *274*, 595–603. [[CrossRef](#)]
2. Sun, T.; Xu, L.; Wang, D.; Li, Y. Metal organic frameworks derived single atom catalysts for electrocatalytic energy conversion. *Nano Res.* **2019**, *12*, 2067–2080. [[CrossRef](#)]
3. Zitolo, A.; Goellner, V.; Armel, V.; Sougrati, M.T.; Mineva, T.; Stievano, L.; Fonda, E.; Jaouen, F. Identification of catalytic sites for oxygen reduction in iron- and nitrogen-doped graphene materials. *Nat. Mater.* **2015**, *14*, 937–942. [[CrossRef](#)] [[PubMed](#)]
4. Borghei, M.; Lehtonen, J.; Liu, L.; Rojas, O.J. Advanced Biomass-Derived Electrocatalysts for the Oxygen Reduction Reaction. *Adv. Mater.* **2018**, *30*, 1703691. [[CrossRef](#)] [[PubMed](#)]
5. Das, S.; Kundu, A.; Kuila, T.; Murmu, N.C. Recent advancements on designing transition metal-based carbon-supported single atom catalysts for oxygen electrocatalysis: Miles to go for sustainable Zn-air batteries. *Energy Storage Mater.* **2023**, *61*, 102890. [[CrossRef](#)]
6. Cui, Q.; Chao, S.J.; Wang, P.H.; Bai, Z.Y.; Yan, H.Y.; Wang, K.; Yang, L. Fe-N/C catalysts synthesized by heat-treatment of iron triazine carboxylic acid derivative complex for oxygen reduction reaction. *RSC Adv.* **2014**, *4*, 12168–12174. [[CrossRef](#)]
7. Wang, R.F.; Li, X.S.; Li, H.; Wang, Q.F.; Wang, H.; Wang, W.; Kang, J.; Chang, Y.M.; Lei, Z.Q. Highly stable and effective Pt/carbon nitride (CN_x) modified SiO₂ electrocatalyst for oxygen reduction reaction. *Int. J. Hydrogen Energy* **2011**, *36*, 5775–5781. [[CrossRef](#)]
8. Yan, L.T.; Yu, J.L.; Houston, J.; Flores, N.; Luo, H.M. Biomass derived porous nitrogen doped carbon for electrochemical devices. *Green Energy Environ.* **2017**, *2*, 84–99. [[CrossRef](#)]
9. Park, S.; Kim, J.; Kwon, K. A review on biomass-derived N-doped carbons as electrocatalysts in electrochemical energy applications. *Chem. Eng. J.* **2022**, *446*, 137116. [[CrossRef](#)]
10. Kundu, A.; Kuila, T.; Murmu, N.C.; Samanta, P.; Das, S. Metal-organic framework-derived advanced oxygen electrocatalysts as air-cathodes for Zn-air batteries: Recent trends and future perspectives. *Mater. Horiz.* **2023**, *10*, 745–787. [[CrossRef](#)]
11. Hu, Y.; Jensen, J.O.; Zhang, W.; Cleemann, L.N.; Xing, W.; Bjerrum, N.J.; Li, Q.F. Hollow Spheres of Iron Carbide Nanoparticles Encased in Graphitic Layers as Oxygen Reduction Catalysts. *Angew. Chem. Int. Ed.* **2014**, *53*, 3675–3679. [[CrossRef](#)] [[PubMed](#)]
12. Shein, I.R.; Medvedeva, N.I.; Ivanovskii, A.L. Electronic and structural properties of cementite-type M₃X (M = Fe, Co, Ni; X = C or B) by first principles calculations. *Phys. B Condens. Matter* **2006**, *371*, 126–132. [[CrossRef](#)]
13. Guo, J.N.; Ning, M.Y.; Xiang, Z.H. Highly efficient iron-nitrogen electrocatalyst derived from covalent organic polymer for oxygen reduction. *J. Energy Chem.* **2017**, *26*, 1168–1173. [[CrossRef](#)]
14. Hu, K.; Tao, L.; Liu, D.D.; Huo, J.; Wang, S.Y. Sulfur-Doped Fe/N/C Nanosheets as Highly Efficient Electrocatalysts for Oxygen Reduction Reaction. *ACS Appl. Mater. Interfaces* **2016**, *8*, 19379–19385. [[CrossRef](#)] [[PubMed](#)]
15. Xue, D.P.; Yuan, P.F.; Jiang, S.; Wei, Y.F.; Zhou, Y.; Dong, C.L.; Yan, W.F.; Mu, S.C.; Zhang, J.N. Altering the spin state of Fe-N-C through ligand field modulation of single-atom sites boosts the oxygen reduction reaction. *Nano Energy* **2023**, *105*, 108020. [[CrossRef](#)]
16. Zeng, R.; Yang, Y.; Feng, X.R.; Li, H.Q.; Gibbs, L.M.; DiSalvo, F.J.; Abruña, H.D. Nonprecious transition metal nitrides as efficient oxygen reduction electrocatalysts for alkaline fuel cells. *Sci. Adv.* **2022**, *8*, eabj1584. [[CrossRef](#)] [[PubMed](#)]
17. Asahi, R.; Morikawa, T.; Ohwaki, T.; Aoki, K.; Taga, Y. Visible-Light Photocatalysis in Nitrogen-Doped Titanium Oxides. *Science* **2001**, *293*, 269–271. [[CrossRef](#)] [[PubMed](#)]
18. Zhu, Y.S.; Zhang, B.S.; Liu, X.; Wang, D.W.; Su, D.S. Unravelling the Structure of Electrocatalytically Active Fe-N Complexes in Carbon for the Oxygen Reduction Reaction. *Angew. Chem. Int. Ed.* **2014**, *53*, 10673–10677. [[CrossRef](#)] [[PubMed](#)]
19. Lu, X.Y.; Li, Y.Q.; Yang, P.X.; Wan, Y.B.; Wang, D.; Xu, H.; Liu, L.L.; Xiao, L.H.; Li, R.P.; Wang, G.Z.; et al. Atomically dispersed Fe-N-C catalyst with densely exposed Fe-N₄ active sites for enhanced oxygen reduction reaction. *Chem. Eng. J.* **2024**, *485*, 149529. [[CrossRef](#)]
20. Gong, K.; Du, F.; Xia, Z.; Durstock, M.; Dai, L. Nitrogen-Doped Carbon Nanotube Arrays with High Electrocatalytic Activity for Oxygen Reduction. *Science* **2009**, *323*, 760–764. [[CrossRef](#)]
21. Jiang, W.J.; Gu, L.; Li, L.; Zhang, Y.; Zhang, X.; Zhang, L.J.; Wang, J.Q.; Hu, J.S.; Wei, Z.D.; Wan, L.J. Understanding the High Activity of Fe-N-C Electrocatalysts in Oxygen Reduction: Fe/Fe₃C Nanoparticles Boost the Activity of Fe-N_x. *J. Am. Chem. Soc.* **2016**, *138*, 3570–3578. [[CrossRef](#)]
22. Sheng, Z.H.; Shao, L.; Chen, J.J.; Bao, W.J.; Wang, F.B.; Xia, X.H. Catalyst-Free Synthesis of Nitrogen-Doped Graphene via Thermal Annealing Graphite Oxide with Melamine and Its Excellent Electrocatalysis. *ACS Nano* **2011**, *5*, 4350–4358. [[CrossRef](#)]
23. Gu, L.Z.; Jiang, L.H.; Jin, J.T.; Liu, J.; Sun, G.Q. Yolk-shell structured iron carbide/N-doped carbon composite as highly efficient and stable oxygen reduction reaction electrocatalyst. *Carbon* **2015**, *82*, 572–578. [[CrossRef](#)]
24. Ye, Y.F.; Li, H.B.; Cai, F.; Yan, C.C.; Si, R.; Miao, S.; Li, Y.S.; Wang, G.X.; Bao, X.H. Two-Dimensional Mesoporous Carbon Doped with Fe-N Active Sites for Efficient Oxygen Reduction. *ACS Catal.* **2017**, *7*, 7638–7646. [[CrossRef](#)]
25. Yan, J.; Gu, T.Y.; Shi, R.H.; Chen, X.; Rummeli, M.H.; Yang, R.Z. Heteroatom sulfur-doping in single-atom Fe-NC catalysts for durable oxygen reduction reaction in both alkaline and acidic media. *J. Mater. Chem. A* **2023**, *11*, 16180–16189. [[CrossRef](#)]
26. Zhou, M.; Yan, S.X.; Wang, Q.; Tan, M.X.; Wang, D.Y.; Yu, Z.Q.; Luo, S.H.; Zhang, Y.H.; Liu, X. Walnut septum-derived hierarchical porous carbon for ultra-high-performance supercapacitors. *Rare Met.* **2022**, *41*, 2280–2291. [[CrossRef](#)]
27. Huang, B.B.; Liu, Y.C.; Xie, Z.L. Biomass derived 2D carbons via a hydrothermal carbonization method as efficient bifunctional ORR/HER electrocatalysts. *J. Mater. Chem. A* **2017**, *5*, 23481–23488. [[CrossRef](#)]

28. Wang, W.; Gong, J.L.; Long, Q.; Wang, H.T.; Huang, J.L.; Dang, W.; Chen, L.; Li, G.Y.; Hou, Z.H.; Xu, W.Y. Fe-Fe₃N composite nitrogen-doped carbon framework: Multi-dimensional cross-linked structure boosting performance for the oxygen reduction reaction electrocatalysis and zinc-air batteries. *Appl. Surf. Sci.* **2023**, *639*, 158218. [[CrossRef](#)]
29. Zhang, Y.P.; Wang, N.; Jia, N.; Wang, J.; Sun, J.; Shi, F.; Liu, Z.H.; Jiang, R.B. A Low-Cost and Facile Method for the Preparation of Fe-N/C-Based Hybrids with Superior Catalytic Performance toward Oxygen Reduction Reaction. *Adv. Mater. Interfaces* **2019**, *6*, 1900273. [[CrossRef](#)]
30. Cui, X.Y.; Yang, S.B.; Yan, X.X.; Leng, J.G.; Shuang, S.; Ajayan, P.M.; Zhang, Z.J. Pyridinic-Nitrogen-Dominated Graphene Aerogels with Fe-N-C Coordination for Highly Efficient Oxygen Reduction Reaction. *Adv. Funct. Mater.* **2016**, *26*, 5708–5717. [[CrossRef](#)]
31. Kim, S.J.; Mahmood, J.; Kim, C.; Han, G.F.; Kim, S.W.; Jung, S.M.; Zhu, G.M.; De Yoreo, J.J.; Kim, G.; Baek, J.B. Defect-Free Encapsulation of Fe⁰ in 2D Fused Organic Networks as a Durable Oxygen Reduction Electrocatalyst. *J. Am. Chem. Soc.* **2018**, *140*, 1737–1742. [[CrossRef](#)] [[PubMed](#)]
32. Kudin, K.N.; Ozbas, B.; Schniepp, H.C.; Prud'homme, R.K.; Aksay, I.A.; Car, R. Raman spectra of graphite oxide and functionalized graphene sheets. *Nano Lett.* **2008**, *8*, 36–41. [[CrossRef](#)] [[PubMed](#)]
33. Gao, S.; Lin, Y.; Jiao, X.C.; Sun, Y.F.; Luo, Q.Q.; Zhang, W.H.; Li, D.Q.; Yang, J.L.; Xie, Y. Partially oxidized atomic cobalt layers for carbon dioxide electroreduction to liquid fuel. *Nature* **2016**, *529*, 68–71. [[CrossRef](#)] [[PubMed](#)]
34. Yan, D.F.; Li, Y.X.; Huo, J.; Chen, R.; Dai, L.M.; Wang, S.Y. Defect Chemistry of Nonprecious-Metal Electrocatalysts for Oxygen Reactions. *Adv. Mater.* **2017**, *29*, 1606459. [[CrossRef](#)] [[PubMed](#)]
35. He, W.H.; Jiang, C.H.; Wang, J.B.; Lu, L.H. High-Rate Oxygen Electroreduction over Graphitic-N Species Exposed on 3D Hierarchically Porous Nitrogen-Doped Carbons. *Angew. Chem. Int. Ed.* **2014**, *53*, 9503–9507. [[CrossRef](#)] [[PubMed](#)]
36. Liang, J.; Du, X.; Gibson, C.; Du, X.W.; Qiao, S.Z. N-Doped Graphene Natively Grown on Hierarchical Ordered Porous Carbon for Enhanced Oxygen Reduction. *Adv. Mater.* **2013**, *25*, 6226–6231. [[CrossRef](#)]
37. Yi, J.D.; Zhang, M.D.; Hou, Y.; Huang, Y.B.; Cao, R. N-Doped Carbon Aerogel Derived from a Metal-Organic Framework Foam as an Efficient Electrocatalyst for Oxygen Reduction. *Chem. Asian J.* **2019**, *14*, 3642–3647. [[CrossRef](#)]
38. Aniruddha, K.; Saikat, B.; Srijib, D.; Haradhan, K.; Chun-Won, K.; Tapas, K.; Naresh Chandra, M. General Approach to Synthesize Multilayer Graphitic Carbon-Nanotube-Encapsulated NiCo Alloys as Trifunctional Electrocatalysts: Deciphering the Role of N-Dopants. *ACS Appl. Energy Mater.* **2022**, *5*, 14445–14454.
39. Guo, D.H.; Shibuya, R.; Akiba, C.; Saji, S.; Kondo, T.; Nakamura, J. Active sites of nitrogen-doped carbon materials for oxygen reduction reaction clarified using model catalysts. *Science* **2016**, *351*, 361–365. [[CrossRef](#)]
40. Zhu, C.; Shi, Q.; Xu, B.Z.; Fu, S.; Wan, G.; Yang, C.; Yao, S.; Song, J.; Zhou, H.; Du, D.; et al. Hierarchically Porous M-N-C (M = Co and Fe) Single-Atom Electrocatalysts with Robust MN_x Active Moieties Enable Enhanced ORR Performance. *Adv. Energy Mater.* **2018**, *8*, 1801956. [[CrossRef](#)]
41. Yamashita, T.; Hayes, P. Analysis of XPS spectra of Fe²⁺ and Fe³⁺ ions in oxide materials. *Appl. Surf. Sci.* **2008**, *254*, 2441–2449. [[CrossRef](#)]
42. Velazquez-Palenzuela, A.; Zhang, L.; Wang, L.C.; Cabot, P.L.; Brillas, E.; Tsay, K.; Zhang, J.J. Carbon-Supported Fe-N_x Catalysts Synthesized by Pyrolysis of the Fe(II)-2,3,5,6-Tetra(2-pyridyl)pyrazine Complex: Structure, Electrochemical Properties, and Oxygen Reduction Reaction Activity. *J. Phys. Chem. C* **2011**, *115*, 12929–12940. [[CrossRef](#)]
43. Liu, Y.Y.; Ruan, J.M.; Sang, S.B.; Zhou, Z.C.; Wu, Q.M. Iron and nitrogen co-doped carbon derived from soybeans as efficient electro-catalysts for the oxygen reduction reaction. *Electrochim. Acta* **2016**, *215*, 388–397. [[CrossRef](#)]
44. Huo, J.J.; Lu, L.; Shen, Z.Y.; Liu, Y.; Guo, J.J.; Liu, Q.B.; Wang, Y.; Liu, H.; Wu, M.H.; Wang, G.X. A rational synthesis of single-atom iron-nitrogen electrocatalysts for highly efficient oxygen reduction reaction. *J. Mater. Chem. A* **2020**, *8*, 16271–16282. [[CrossRef](#)]
45. Zhang, D.; Ding, R.X.; Zhang, C.Q.; Tang, Y.Z.; Yuan, T.J.; Dong, Q.P.; Bi, L.S.; Shi, S.; He, Y. Efficient Synthesis of Fe/N-Doped Carbon Nanotube as Highly Active Catalysts for Oxygen Reduction Reaction in Alkaline Media. *Langmuir* **2022**, *38*, 9310–9320. [[CrossRef](#)]

Disclaimer/Publisher's Note: The statements, opinions and data contained in all publications are solely those of the individual author(s) and contributor(s) and not of MDPI and/or the editor(s). MDPI and/or the editor(s) disclaim responsibility for any injury to people or property resulting from any ideas, methods, instructions or products referred to in the content.